Real-time turbulence profiling with a pair of laser guide star Shack–Hartmann wavefront sensors for wide-field adaptive optics systems on large to extremely large telescopes

L. Gilles* and B. L. Ellerbroek

Thirty Meter Telescope Observatory Corporation, 1200 E. California Boulevard, Mail Code 102-8, Pasadena, California 91125, USA
*Corresponding author: lgilles@caltech.edu

Real-time turbulence profiling is necessary to tune tomographic wavefront reconstruction algorithms for wide-field adaptive optics (AO) systems on large to extremely large telescopes, and to perform a variety of image post-processing tasks involving point-spread function reconstruction. This paper describes a computationally efficient and accurate numerical technique inspired by the slope detection and ranging (SLODAR) method to perform this task in real time from properly selected Shack–Hartmann wavefront sensor measurements accumulated over a few hundred frames from a pair of laser guide stars, thus eliminating the need for an additional instrument. The algorithm is introduced, followed by a theoretical influence function analysis illustrating its impulse response to high-resolution turbulence profiles. Finally, its performance is assessed in the context of the Thirty Meter Telescope multi-conjugate adaptive optics system via end-to-end wave optics Monte Carlo simulations. © 2010 Optical Society of America

OCIS codes: 010.1080, 010.7350, 010.1330.

1. INTRODUCTION

An integral part of current and next generation ground-based astronomical telescopes are laser guide star (LGS) adaptive optics (AO) systems. Many systems will utilize multiple mesospheric sodium LGSs in order to implement laser tomography for ground-layer adaptive optics (GLAO), laser tomography adaptive optics (LTAO), multi-object adaptive optics (MOAO) or multi-conjugate adaptive optics (MCAO) [1–5]. Real-time turbulence profiling is necessary for these wide-field AO systems to tune their tomographic wavefront reconstruction algorithm [6,7] and perform a variety of image post-processing tasks involving point-spread function reconstruction [8]. This paper describes a computationally efficient and accurate numerical technique inspired by the slope detection and ranging (SLODAR) method [9–13] to perform this task in real-time from properly selected Shack–Hartmann wavefront sensor (WFS) measurements accumulated over a few hundred frames from a pair of LGSs, thus eliminating the need for an additional instrument. A somewhat similar SLODAR-like technique was presented earlier in 2010 [14]. Of course, turbulence sensing with crossed beams has been known for some time [15]. The main conclusions of our analysis are the following:

1. Sensitivity of the method to global tip/tilt and focus can be eliminated by correlating the local curvature of WFS measurements, a feature desirable on account of the uncertain position of LGSs [16] and spatio-temporal fluctuations of the mesospheric sodium layer [17].

2. Turbulence profiling is intrinsically performed at nonequispaced layer altitudes given by

$$h_k = \frac{d_k}{\theta + d_k/H},\tag{1}$$

where k denotes layer index ($k = 0, 1, \cdots, n_l - 1$), $d_k = k\Delta$ denotes baseline number k used by the SLODAR-like algorithm, Δ is the LGS WFS subaperture size, $\theta > 0$ is the relative angular separation between the LGS pair (assumed to be either along the x or y direction without loss of generality), and H is the mean altitude of the LGS pair.

3. Resampling of the turbulence profile estimate computed at altitudes given by Eq. (1) to arbitrary altitudes can be performed if necessary by application of a downsampling matrix computed with triangular [multi-aperture scintillation sensor (MASS)-like] interpolating functions. Fine vertical sampling (achieved with a widely separated LGS pair) is, however, desirable for wide-field AO concepts to reduce the requirement for accurate knowledge of layer altitudes [18].

4. Relative estimation errors in the Fried parameter r_0, the isoplanatic angle θ_0, and the generalized dual-conjugate isoplanatic angle θ_2 [19] are all within a few percent after a few hundred frames of accumulated measurements.

The paper has been structured as follows. Section 2 discusses the proposed SLODAR-like numerical technique, including changes made to the standard method for use

with LGSs. Section 3 presents a theoretical influence function analysis illustrating the impulse response of the method to high-resolution turbulence profiles. Finally, performance is assessed in Section 4 in the context of the Thirty Meter Telescope (TMT) MCAO system via end-to-end wave optics Monte Carlo simulations. Section 5 concludes the study.

2. SLODAR-LIKE METHOD

A. Preliminaries
In what follows, atmospheric turbulence has been discretized into layers at arbitrary altitudes h_k [not necessarily given by Eq. (1)] separated by $\Delta_k = h_{k+1} - h_k$. Each layer represents an optical wavefront, i.e., an optical path difference (OPD) in units of meters ϕ_k, and is fully characterized by its second-order statistics expressed as a structure function, covariance matrix, or power spectral density (PSD), all proportional to the layer strength:

$$p_k = \frac{r_{0,k}^{-5/3}}{(2\pi/\lambda)^2} = 0.423 \int_{h_{k-1}}^{h_{k+1}} C_n^2(h) H_k(h) dh, \qquad (2)$$

where $r_{0,k}$ denotes the Fried parameter for layer k, and $H_k(h)$ is a triangular MASS-like interpolating function given by

$$H_k(h) = \begin{cases} 1 - |h - h_k|/\Delta_k, & \text{if } h_k \leq h \leq h_{k+1} \\ 1 - |h - h_k|/\Delta_{k-1}, & \text{if } h_{k-1} \leq h \leq h_k \\ 0, & \text{else} \end{cases} \qquad (3)$$

Note that p_k is wavelength independent. Equation (2) can be rewritten in matrix form by discretizing the integral using a quadrature integration rule (e.g., a trapezoidal or Simpson's rule):

$$\vec{p} = H\vec{p}', \qquad (4)$$

$$\vec{p}' = W\vec{y}, \qquad (5)$$

where $H_{kl} = H_k(h = h_l)$, W denotes a square diagonal matrix containing the quadrature interpolating weights multiplied by 0.423, and $\vec{y}$ is a vector of C_n^2 values. Each column of H should have unit L_1 norm in order to preserve the total turbulence strength (L_1 norm of $\vec{p}'$).

It is useful to associate to the strength vector $\vec{p}$ the following four turbulence parameters: the global Fried parameter r_0, the isoplanatic angle θ_0, the generalized isoplanatic angle for a MCAO system with two deformable mirrors (DMs) respectively conjugate to $h=0$ and $h=h_{DM}$, θ_2, and the Greenwood frequency f_G. These parameters can be evaluated from the following expressions:

$$r_0^{-5/3} = \sum_k r_{0,k}^{-5/3}, \qquad (6)$$

$$\theta_0^{-5/3} = \sum_k \theta_{0,k}^{-5/3}, \qquad (7)$$

$$\frac{\theta_{0,k}^{-5/3}}{(2\pi/\lambda)^2} = \left(\frac{2.914}{0.423}\right) p_k h_k^{5/3}, \qquad (8)$$

$$\theta_2^{-5/3} = \sum_k \theta_{2,k}^{-5/3}, \qquad (9)$$

$$\frac{\theta_{2,k}^{-5/3}}{(2\pi/\lambda)^2} = \left(\frac{2.914}{0.423}\right) p_k F_2(h_k), \qquad (10)$$

$$F_2(h_k) = \frac{h_k^{5/3}}{2} + \frac{|h_k - h_{DM}|^{5/3}}{2} - \frac{h_{DM}^{5/3}}{4}$$
$$- \frac{h_{DM}^{-5/3}}{4}(h_k^{5/3} - |h_k - h_{DM}|^{5/3})^2, \qquad (11)$$

$$f_G^{5/3} = \sum_k f_{G,k}^{5/3}, \qquad (12)$$

$$\frac{f_{G,k}^{5/3}}{(2\pi/\lambda)^2} = \left(\frac{0.102}{0.423}\right) p_k v_k^{5/3}, \qquad (13)$$

where v_k denotes wind speed at altitude h_k. In what follows, all of these turbulence parameters will be quoted at a wavelength λ of 500 nm.

The proposed method for real-time estimation of $\vec{p}$ with a pair of LGS WFSs is targeted toward tuning of the tomographic wavefront reconstruction algorithms used by laser tomography AO systems (GLAO, LTAO, MOAO, MCAO). These wavefront reconstruction algorithms incorporate the covariance matrix of ϕ_k (or its inverse, depending on algorithm formulation), which is proportional to p_k [6,7].

B. Measurement Description
The geometry of the SLODAR technique is illustrated in Fig. 1 for a pair of natural guide stars (NGSs) with angular coordinates $\vec{\varphi} = (\varphi, 0)$ and $\vec{\varphi}' = (\varphi', 0)$. The relative angular coordinate is $\vec{\theta} = (\theta = \varphi - \varphi', 0)$. The fact that $\theta > 0$ en-
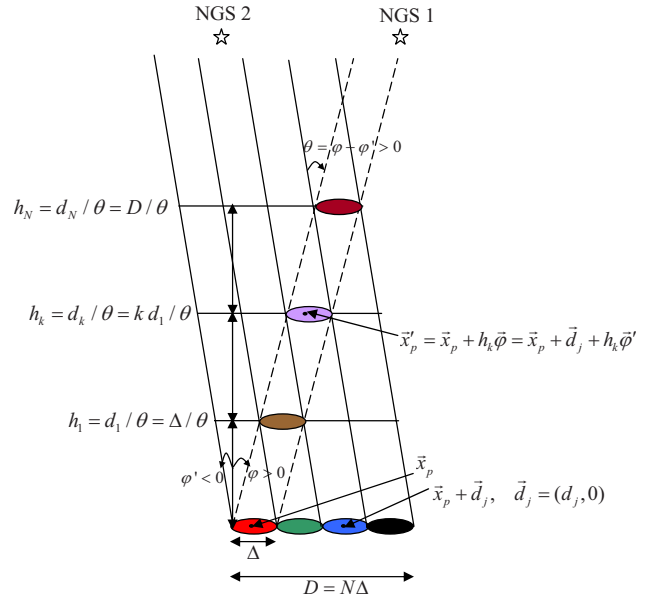

Fig. 1. (Color online) Illustration of the geometry of the SLODAR technique for a pair of NGS Shack–Hartmann WFSs. θ denotes the relative angular coordinate of the NGS pair and Δ the NGS WFS subaperture size.

sures that both beams cross at a positive altitude. For this geometry, turbulence profile estimation is performed at equispaced layer altitudes given by $h_k = d_k/\theta$, which is the limit case of Eq. (1) when $H \to \infty$. $\vec{x}_p$ denotes a selected subaperture coordinate on the first WFS and $\vec{x}_p + \vec{d}_j$ a selected coordinate on the second WFS. $\vec{d}_j = (d_j, 0)$ is the baseline vector j, chosen such that the pair of rays connecting $\vec{x}_p$ to the first NGS and $\vec{x}_p + \vec{d}_j$ to the second NGS intersect at altitude h_k, which occurs for the choice $\vec{d}_j = h_k \vec{\theta}$, i.e., when the projected baseline at altitude h_k is null: $\vec{d}_j' = \vec{d}_j - h_k \vec{\theta} = \vec{0}$.

The proposed turbulence profile estimation technique follows the same geometry as in Fig. 1 with the only difference being the use of finite range guide stars. The essence of the technique is to fit accumulated measured covariances between properly selected measurements from a pair of LGS WFSs to a correlation model. Note that in closed-loop contexts, LGS WFS measurements need to be converted into "pseudo-open loop" measurements [7], i.e., partially recovered open-loop gradients obtained by adding to the closed-loop measurements the gradients produced by the DM commands (modeled using a geometric interation matrix).

In order to introduce the correlation model, we start by expressing a gradient measurement along the α (either x or y) direction $s_\alpha(\vec{x}_p)$ on a selected square fully illuminated WFS subaperture at coordinate $\vec{x}_p$ looking at an angle $\vec{\varphi} = (\varphi, 0)$ as a sum over contributions from each turbulence layer:

$$s_\alpha(\vec{x}_p) = \frac{1}{\Delta^2} \sum_k \int \mathrm{rec}\left(\frac{\vec{x} - \vec{x}_p}{\Delta}\right) \frac{\partial}{\partial \alpha} \phi_k(\xi_k \vec{x} + h_k \vec{\varphi}) d^2\vec{x}, \tag{14}$$

where $\vec{x}$ denotes the aperture-plane coordinates, and $\xi_k = 1 - h_k/H < 1$ denotes the cone compression factor for a LGS at altitude H and a layer at altitude h_k. s_α has units of angle (OPD separation over subaperture size). Rewriting Eq. (14) in terms of the aperture-plane coordinates projected onto atmospheric layer k, $\vec{x}' = \xi_k \vec{x} + h_k \vec{\varphi}$, yields

$$s_\alpha(\vec{x}_p) = \frac{1}{\Delta^2} \sum_k \int \omega_k^\alpha(\vec{x}') \phi_k(\vec{x}' + \vec{x}_p') d^2\vec{x}', \tag{15}$$

$$\omega_k^\alpha(\vec{x}') = \frac{1}{\xi_k} \mathrm{rec}\left(\frac{\vec{x}'}{\xi_k \Delta}\right) \frac{\partial}{\partial \alpha'}. \tag{16}$$

Since global tip/tilt and focus are poorly measured by LGS WFSs on account of LGS angular position and range uncertainty [16,17], it is necessary to correlate a local curvature (i.e., second-order difference) of gradients to eliminate sensitivity to these modes. This differencing operation is performed on the measurements from three adjacent subapertures as follows:

$$m_\alpha(\vec{x}_p) = s_\alpha(\vec{x}_p - \vec{\delta}_\alpha) - 2 s_\alpha(\vec{x}_p) + s_\alpha(\vec{x}_p + \vec{\delta}_\alpha), \tag{17}$$

where $\vec{\delta}_\alpha = (\Delta, 0)$ when $\alpha = x$, and $\vec{\delta}_\alpha = (0, \Delta)$ when $\alpha = y$. Substituting Eq. (15) into Eq. (17) yields

$$m_\alpha(\vec{x}_p) = \frac{1}{\Delta^2} \sum_k \int \mu_k^\alpha(\vec{x}') \phi_k(\vec{x}' + \vec{x}_p') d^2\vec{x}', \tag{18}$$

$$\mu_k^\alpha(\vec{x}') = \omega_k^\alpha(\vec{x}' - \xi_k \vec{\delta}_\alpha) - 2\omega_k^\alpha(\vec{x}') + \omega_k^\alpha(\vec{x}' + \xi_k \vec{\delta}_\alpha). \tag{19}$$

C. Measurement Covariances

It is convenient to rewrite Eq. (18) in the Fourier domain:

$$m_\alpha(\vec{x}_p) = \frac{1}{\Delta^2} \sum_k \int \widehat{\mu_k^\alpha}(\vec{f}') \widehat{\phi_k}(\vec{f}') \exp(2i\pi \vec{f}'^\mathrm{T} \vec{x}_p'), \tag{20}$$

where the Fourier transformed kernel functions are given by

$$\widehat{\mu_k^\alpha}(\vec{f}') = 2\widehat{\omega_k^\alpha}(\vec{f}')[\cos(2\pi \vec{f}'^\mathrm{T} \xi_k \vec{\delta}_\alpha) - 1], \tag{21}$$

$$\widehat{\omega_k^\alpha}(\vec{f}') = -2i\pi f_\alpha' \frac{(\xi_k \Delta)^2}{\xi_k} \mathrm{sinc}(f_x' \xi_k \Delta) \mathrm{sinc}(f_y' \xi_k \Delta). \tag{22}$$

The correlation model between measurement $m_\alpha(\vec{x}_p)$ obtained on the first WFS and $m_\alpha'(\vec{x}_p + \vec{d}_j)$ on the second WFS looking at an angle $\vec{\varphi}' = (\varphi', 0)$ with $\theta = \varphi - \varphi' > 0$ can now be formulated as follows:

$$\langle m_\alpha(\vec{x}_p) m_\alpha'(\vec{x}_p + \vec{d}_j) \rangle = \sum_k A_{jk}^\alpha p_k, \tag{23}$$

where the matrix element A_{jk}^α cross-coupling baseline j to layer k is given by

$$A_{jk}^\alpha = \int d^2 \vec{f}' |\widehat{\mu_k^\alpha}(\vec{f}')|^2 \mathrm{PSD}_0(\vec{f}') \exp(2i\pi \vec{f}'^\mathrm{T} \vec{d}_j'), \tag{24}$$

$$\mathrm{PSD}_0(\vec{f}') = 2.29 \times 10^{-2} (\|\vec{f}'\|^2 + L_0^{-2})^{-11/6}, \tag{25}$$

where $\vec{d}_j' = \xi_k \vec{d}_j - h_k \vec{\theta}$. In other words, A_{jk}^α, is expressed as an inverse Fourier transform of a filtered unit strength von Kármán PSD evaluated at the projected baseline coordinate $\vec{d}_j'$. Since A is a small matrix, each matrix element (24) can be numerically evaluated as a double summation of the discretized integrand. As illustrated in Fig. 1, when the relative LGS angular coordinate is either along the x or y direction (a requirement that can be incorporated into the opto-mechanical design of the system by maintaining a fixed LGS asterism orientation in the LGS WFS coordinate system), a natural choice of layer altitudes h_k at which turbulence strength will be estimated is that given in Eq. (1). For this choice of altitudes, we have

$$d_j' = \left[j - k\left(\frac{1 + j\Delta/(\theta H)}{1 + k\Delta/(\theta H)}\right)\right]\Delta. \tag{26}$$

Note that Eqs. (24) and (26) indicate that A^α is nonsymmetric for finite range guide stars ($H < \infty$) and becomes symmetric in the limit $H \to \infty$. Note also that measurement noise is uncorrelated between distinct WFSs, and hence measurement noise statistics does not appear in Eq. (24).

D. Turbulence Profile Estimation

Finally, Eq. (23) leads to a matrix system of the form $A^\alpha \vec{p} = \vec{b}^\alpha$, where $\vec{b}^\alpha$ denotes the vector of measured correlations with the jth component equal to

$$[\vec{b}^\alpha]_j = \left(\frac{1}{n_p}\right) \sum_{p=1}^{n_p} \langle m_\alpha(\vec{x}_p) m'_\alpha(\vec{x}_p + \vec{d}_j) \rangle, \qquad (27)$$

where n_p denotes the total number of valid subapertures over which the correlations are averaged. The size of A^α is thus equal to $n_d \times n_l$, where n_d denotes the number of baseline vectors $\vec{d}_j$ used and n_l the number of reconstructed layers. Note that $n_d = n_l$ when altitudes are selected as in Eq. (1). Concatenating the above $\alpha = x$ and $\alpha = y$ matrix systems leads to the augmented system $A\vec{p} = \vec{b}$, where A has size $2n_d \times n_l$. The solution $\hat{p}$ of this overdetermined system is given by the least-squares projection of $\vec{b}$ onto the range of A:

$$\hat{p} = \arg \min_{\vec{p}} \|A\vec{p} - \vec{b}\|^2 = A^\dagger \vec{b}, \qquad (28)$$

$$A^\dagger = (A^T A)^{-1} A^T. \qquad (29)$$

Note that Eq. (28) does not guarantee non-negativity of the solution vector. When negative entries occur, these components are set to zero, and the minimization is repeated for the reduced-size system obtained by removing the corresponding columns of A.

3. INFLUENCE FUNCTION ANALYSIS

In order to analyze the response of the above discrete estimator $A^\dagger$ to high-resolution turbulence profiles, we first compute $A^\dagger$ for a small number n_l of altitudes selected as in Eq. (1) using $n_d = n_l$ baselines $d_j = j\Delta$ with $j = 0, \cdots, n_l - 1$. A down-sampling matrix can then be formed by postmultiplication of $A^\dagger$ with a high-resolution kernel B computed for a much larger number of turbulence altitudes, but with the same baselines d_j used to build the lower resolution kernel A. We will call influence functions the columns of the down-sampling matrix $Q = A^\dagger B$, since they quantify how a given input unit strength layer on a finely sampled altitude grid is estimated by $A^\dagger$ on a coarser grid.

This procedure has been carried out for $A^\dagger$ estimating turbulence on either $n_l = 6$ or $n_l = 12$ layers at altitudes selected as in Eq. (1) with $\Delta = 0.5$ m and $\theta = 35''$ for the 6-layer case and $\theta = 67''$ for the 12-layer case, and for B computed for 27 layers. For the 12-layer case, Q has been pre-multiplied by H as given in Eq. (3) to form a 6-layer estimate. The chosen values of θ correspond to two possible LGS pairs from the TMT $70''$ diameter 6-LGS asterism (pentagon+on-axis) [1]. The resulting 27 influence functions are displayed in Fig. 2 for the $\theta = 35''$ case, and in Fig. 3 for the $\theta = 67''$ case. It is seen that each influence function has non-zero weights at the selected 6 layer altitudes, and that both narrow and wide LGS separations produce similar influence functions. Slightly negative weights are also observed in the tails of these influence functions, a feature (probably introduced by discretization effects) that is unphysical since each p_k should be nonnegative.
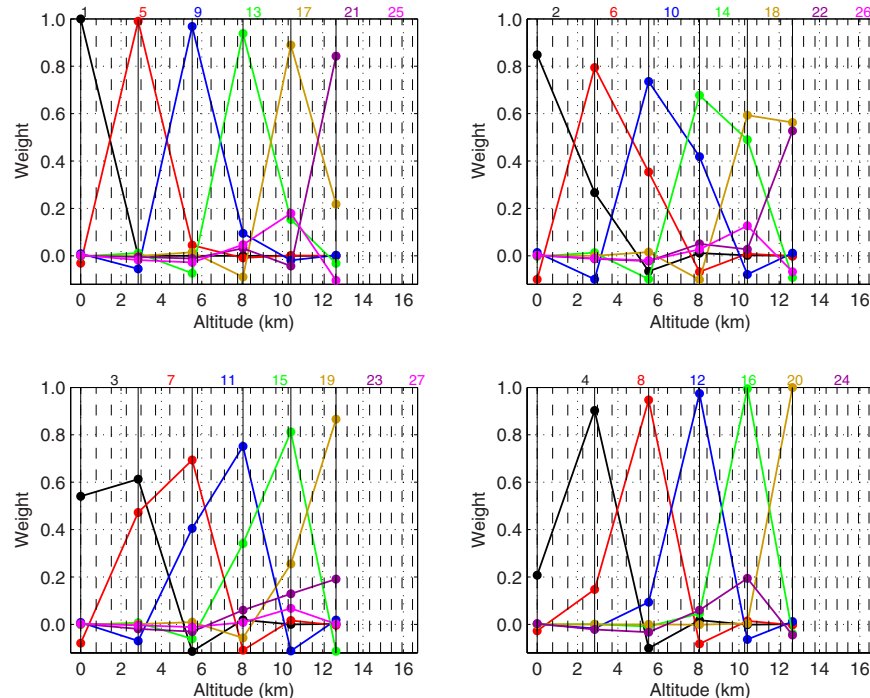

Fig. 2. (Color online) Sample influence functions (columns of $Q = A^\dagger B$) illustrating how a 27-layer turbulence profile is sensed at six altitudes selected as in Eq. (1) with $\Delta = 0.5$ m and $\theta = 35''$. The 27 influence functions have been grouped into four panels. The numbers at the top of each panel indicate which influence is plotted and the location of the corresponding layer, and they provide a color-coded pointer to the corresponding influence function.
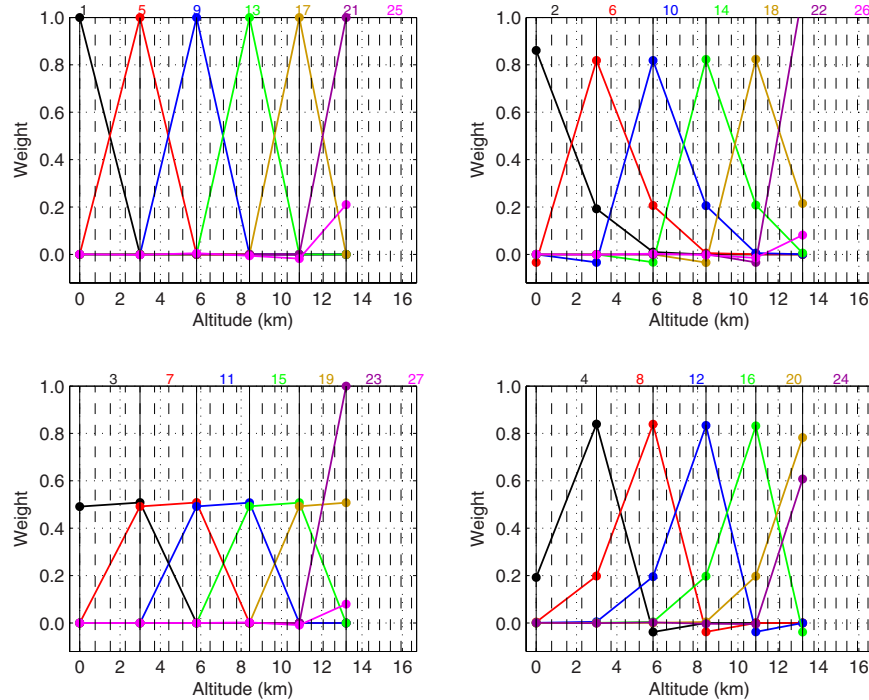
Fig. 3.   (Color online) Same as in Fig. 2 but for $A^{\dagger}$ estimating turbulence at 12 altitudes selected as in Eq. (1) with $\Delta=0.5$ m and $\theta=67''$, followed by down-sampling to six layers via Eq. (4).

4. SAMPLE SIMULATION RESULTS

Detailed Monte Carlo simulations were conducted in order to test the accuracy of the proposed method in the context of the TMT MCAO system [1], which is an order 60×60 wavefront sensing and order 63×63 correction on the ground conjugated deformable mirror (DM) and order 76×76 correction on the $h_{\mathrm{DM}}=11.2$ km conjugated DM. Our study has been performed for high-resolution simulated turbulence profiles obtained from generalized scintillation detection and ranging (SCIDAR) measurements over Mauna Kea during four nights in 2002 [20]. Two sample profiles corresponding to a median r_0 are displayed in Fig. 4 as dimensionless relative weights $\omega_k = p_k/\Sigma_k p_k$. The $N=65$-layer profile was directly obtained from generalized SCIDAR measurements, whereas the $N=27$-layer profile was obtained from the former by application of the down-sampling matrix given in Eq. (3). Both profiles are characterized by $r_0=0.18$ m, $\theta_0=2.8''$, and $\theta_2(h_{\mathrm{DM}}=11.2$ km$)=10.9''$ at $\lambda=500$ nm. High-resolution night-time wind profiles were obtained from the NCEP/NCAR (National Center for Environmental Prediction/Atmospheric Research) reanalysis project [21]. The Greenwood frequency associated with the two profiles displayed in Fig. 4 is $f_{\mathrm{G}}=22$ Hz at $\lambda=500$ nm.

Both the 65-layer and 27-layer turbulence profiles displayed in Fig. 4 were simulated. Phase screens were generated via fast Fourier transforms (FFTs) on 4096×4096 grids sampled at $1/64$ m with $L_0=30$ m outer scale. All simulations included the effects of LGS WFS measurement noise and LGS WFS nonlinearity resulting from the use of a constrained matched filter centroiding algorithm [22].

The TMT MCAO tomographic wavefront reconstruction algorithm is required to reconstruct $n_l=6$ turbulence lay-

ers [7]. Tuning of the weight vector $\vec{p}$ of these layers was achieved by periodic update of this vector every 100 frames, starting 400 frames after the LGS loop running at 800 Hz had been closed. The update was provided by the previously described SLODAR-like algorithm. An intentional mistuning of $\vec{p}$ used by the tomography algorithm at the beginning of the simulation was performed in order to provide insight into the required number of frames to accumulate the SLODAR covariances to yield optimal closed-loop performance.

Figure 5 displays results for the simulated 27-layer atmosphere and for the SLODAR algorithm using the nar-
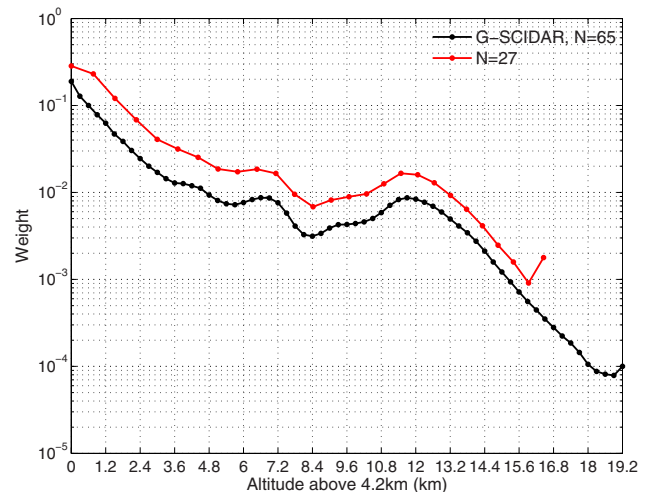

Fig. 4.   (Color online) Median seeing Mauna Kea atmospheric turbulence profiles obtained from [20]. The 65-layer profile was obtained from generalized SCIDAR, while the 27-layer one was generated by application of the MASS-like down-sampling matrix Eq. (4) to the former profile.
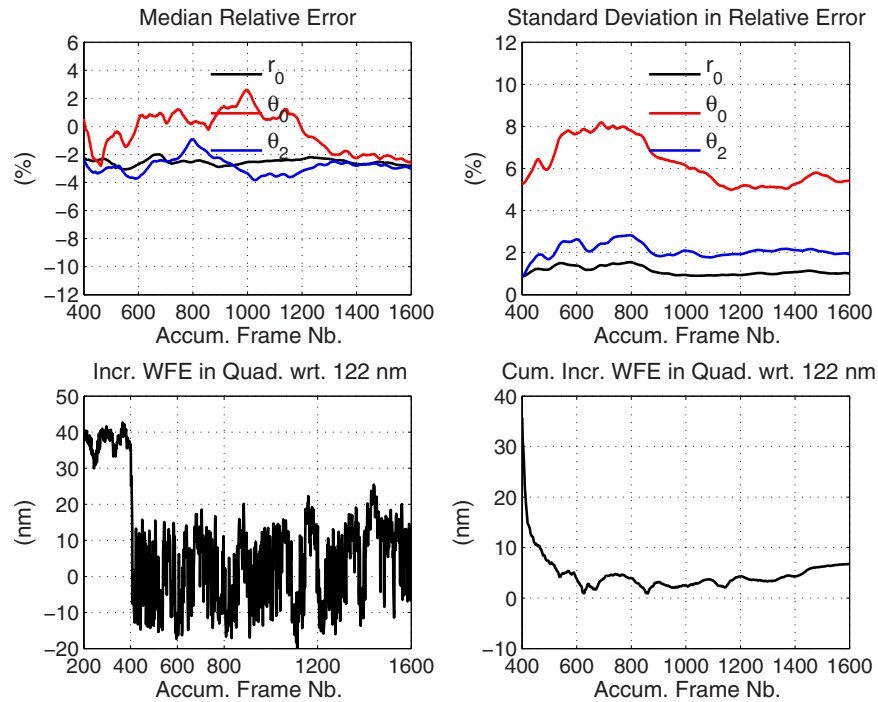
Fig. 5. (Color online) Results for the simulated 27-layer atmosphere and for the SLODAR-like algorithm using the narrow LGS pair separated by $\theta = 35''$. Upper panels illustrate the time history of the median and standard deviation of the relative estimation error in r_0, θ_0, and θ_2 over five different normally distributed realizations of the atmosphere. Bottom panels illustrate the time history of the residual WFE and of its cumulative temporal average delivered by the TMT MCAO system and plotted as incremental WFE in quadrature with respect to a performance estimate of 122 nm RMS obtained in simulations where the reconstruction algorithm is well tuned to the turbulence profile. Positive values indicate degraded performance (higher WFE) compared to 122 nm, while negative values indicate improved performance (lower WFE).

row LGS pair separated by $\theta = 35''$. Upper panels illustrate the time history of the median and standard deviation of the relative estimation error in r_0, θ_0, and θ_2 over five different normally distributed realizations of the atmosphere. It is seen that all of these errors are within a

few percent. Bottom panels illustrate the time history of the residual wavefront error (WFE) and of its cumulative temporal average delivered by the MCAO system and plotted as incremental WFE in quadrature with respect to a performance estimate of 122 nm root-mean-square
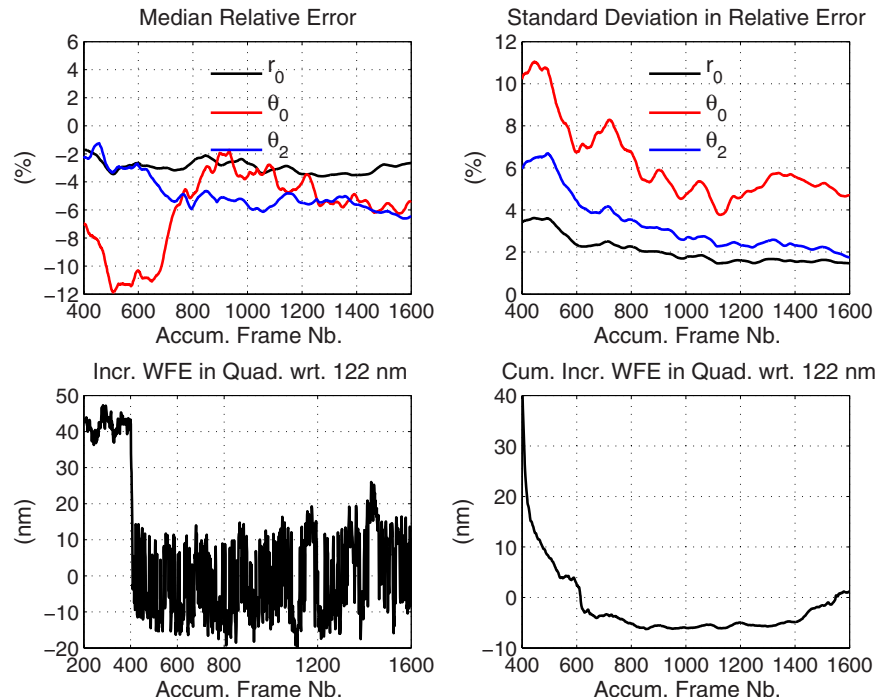

Fig. 6. (Color online) Same as in Fig. 5 but with the SLODAR-like algorithm employing the wider LGS pair separated by $\theta = 67''$.
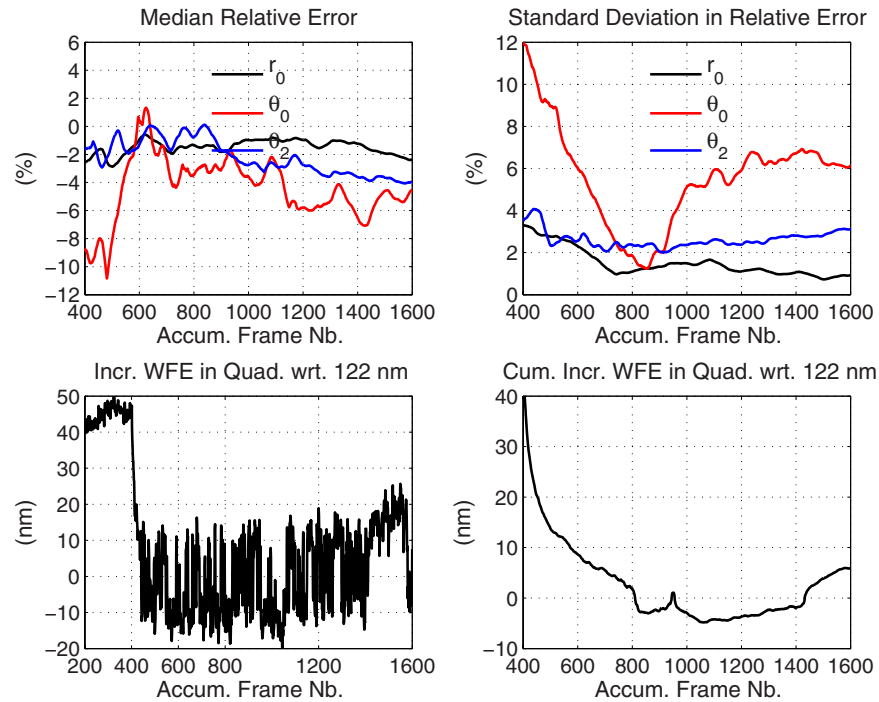
Fig. 7.   (Color online) Same as in Fig. 6 but for the simulated 65-layer atmosphere.

(RMS) obtained in simulations where the reconstruction algorithm is well tuned to the turbulence profile. Positive values indicate degraded performance (higher WFE) compared to 122 nm, while negative values indicate improved performance (lower WFE). Note that this performance estimate does not include implementation errors and tip/tilt and tilt anisoplanatism errors [23]. It is seen that only a few hundred accumulation frames are needed for optimal closed-loop residual WFE. Figure 6 illustrates results for the same scenario as in Fig. 5 but with the SLODAR algorithm employing the wider LGS pair separated by θ =67″. Results are similar to those obtained for the narrower LGS pair with the caveat that a longer accumulation time may be required on account of the wider baselines used in this case. Finally, Fig. 7 illustrates results for the same scenario as in Fig. 6 but for the simulated 65-layer atmosphere. Results are also very similar to those obtained for the simulated 27-layer atmosphere.

5. CONCLUSIONS

We have described a computationally efficient and accurate numerical technique requiring a short averaging time inspired by the SLODAR method to tune tomographic wavefront reconstruction algorithms for wide-field adaptive optics systems on large to extremely large telescopes, and to perform a variety of image post-processing tasks involving point-spread function reconstruction. We have shown that this task can be performed in real time from properly selected Shack–Hartmann WFS measurements from a pair of LGSs, eliminating the need for an additional instrument.

REFERENCES

1. B. Ellerbroek, S. Adkins, D. Andersen, J. Atwood, S. Browne, C. Boyer, P. Byrnes, K. Caputa, R. Conan, R. Cousty, D. Erikson, J. Fitzsimmons, F. Gamache, L. Gilles, G. Herriot, P. Hickson, O. Lardiere, P. Morin, J. Pazder, T. Pfrommer, D. Quinn, V. Reshetov, S. Roberts, J.-C. Sinquin, M. Schoeck, M. Smith, G. Tyler, J. Vaughn, J.-P. Véran, C. Vogel, L. Wang, and I. Wevers, "First light adaptive optics systems and components for the Thirty Meter Telescope," Proc. SPIE **7736**, 773604-1–773604-14 (2010).
2. P. Hinz, A. Bouchez, M. Johns, S. Shectman, M. Hart, B. McLeod, and P. McGregor, "The GMT adaptive optics system," Proc. SPIE **7736**, 77360C-1–77360C-12 (2010).
3. T. Fusco, Y. Cl'enet, S. Meimon, M. Cohen, J. Paufique, C. Petit, D. Gratadour, V. Michau, J.-P. Amans, J.-L. Dournaux, P. Jagourel, H. Schnetler, J.-M. Conan, C. Robert, E. Gendron, G. Rousset, and N. Hubin, "ATLAS: the laser tomographic adaptive optics module for the E-ELT," in *Proceedings of 1st AO4ELT Conference—Adaptive Optics for Extremely Large Telescopes* (EDP Sciences, 2010), pp. 02002-1–02002-6, available online at ao4elt.edpsciences.org.
4. E. Diolaiti, J.-M. Conan, I. Foppiani, M. Lombini, E. Marchetti, C. Petit, C. Robert, L. Schreiber, A. Baruffolo, M. Bellazzini, G. Bregoli, P. Ciliegi, G. Cosentino, V. Biliotti, S. D'Odorico, T. Fusco, N. Hubin, S. Meimon, and J.-F. Sauvage, "Towards the phase A review of MAORY, the multiconjugate adaptive optics module for the E-ELT," in *Pro-*

ceedings of 1st AO4ELT Conference—Adaptive Optics for Extremely Large Telescopes (EDP Sciences, 2010), pp. 02007-1–02007-5, available online at ao4elt.edpsciences.org.

5. G. Rousset, T. Fusco, F. Assemat, T. Morris, E. Gendron, R. Myers, M. Brangier, M. Cohen, N. Dipper, C. Evans, D. Gratadour, P. Jagourel, P. Laporte, D. Le Mignant, M. Puech, C. Robert, H. Schnetler, W. Taylor, F. Vidal, J.-G. Cuby, M. Lehnert, S. Morris, and P. Parr-Burmann, "EAGLE multi-object AO concept study for the E-ELT," in Proceedings of 1st AO4ELT Conference—Adaptive Optics for Extremely Large Telescopes (EDP Sciences, 2010), pp. 02008-1–02008-6, available online at ao4elt.edpsciences.org.

6. T. Fusco, J.-M. Conan, G. Rousset, L. M. Mugnier, and V. Michau, "Optimal wavefront reconstruction strategies for multiconjugate adaptive optics," J. Opt. Soc. Am. A 18, 2527–2538 (2001).

7. L. Gilles and B. L. Ellerbroek, "Split atmospheric tomography using laser and natural guide stars," J. Opt. Soc. Am. A 25, 2427–2435 (2008).

8. M. C. Britton, "The anisoplanatic point-spread function in adaptive optics," Publ. Astron. Soc. Pac. 118, 885–900 (2006).

9. R. W. Wilson, "Slodar: measuring optical turbulence altitude with a Shack–Hartmann wavefront sensor," Mon. Not. R. Astron. Soc. 337, 103–108 (2002).

10. T. Butterley, R. W. Wilson, and M. Sarazin, "Determination of the profile of atmospheric optical turbulence strength from SLODAR data," Mon. Not. R. Astron. Soc. 369, 835–845 (2006).

11. N. Védrenne, V. Michau, C. Robert, and J.-M. Conan, "C_n^2 profile measurement from Shack–Hartmann data," Opt. Lett. 32, 2659–2661 (2007).

12. L. Wang, M. Schöck, and G. Chanan, "Atmospheric turbulence profiling with SLODAR using multiple adaptive optics wavefront sensors," Appl. Opt. 47, 1880–1892 (2008).

13. M. Goodwin, C. Jenkins, and A. Lambert, "Improved detection of atmospheric turbulence with SLODAR," Opt. Express 15, 14845–14860 (2007).

14. F. Vidal, E. Gendron, M. Brangier, A. Sevin, G. Rousset, and Z. Hubert, "Tomography reconstruction using the Learn and Apply algorithm," in Proceedings of 1st AO4ELT Conference—Adaptive Optics for Extremely Large Telescopes (EDP Sciences, 2010), pp. 07001-1–07001-6, available online at ao4elt.edpsciences.org.

15. A. Tokovinin and E. Viard, "Limiting precision of tomographic phase estimation," J. Opt. Soc. Am. A 18, 873–882 (2001).

16. F. Rigaut and E. Gendron, "Laser guide star in adaptive optics: the tilt determination problem," Astron. Astrophys. 262, 677–684 (1992).

17. T. Pfrommer, P. Hickson, and C. Y. She, "A large-aperture sodium fluorescence lidar with very high resolution for mesopause dynamics and adaptive optics studies," Geophys. Res. Lett. 36, L15831 (2009).

18. B. Neichel, T. Fusco, and J.-M. Conan, "Tomographic reconstruction for wide-field adaptive optics systems: Fourier domain analysis and fundamental limitations," J. Opt. Soc. Am. A 26, 219–235 (2009).

19. A. Tokovinin, M. Le Louarn, and M. Sarazin, "Isoplanatism in multiconjugate adaptive optics system," J. Opt. Soc. Am. A 17, 1819–1827 (2000).

20. A. Tokovinin, J. Vernin, A. Ziad, and M. Chun, "Optical turbulence profiles at Mauna Kea measured by MASS and SCIDAR," Publ. Astron. Soc. Pac. 117, 395–400 (2005).

21. E. Kalnay, M. Kanamitsu, R. Kistler, W. Collins, D. Deaven, L. Gandin, M. Iredell, S. Saha, G. White, J. Woollen, Y. Zhu, A. Leetmaa, R. Reynolds, M. Chelliah, W. Ebisuzaki, W. Higgins, J. Janowiak, K. C. Mo, C. Ropelewski, J. Wang, R. Jenne, and D. Joseph, "The NCEP/NCAR 40-year reanalysis project," Bull. Am. Astron. Soc. 77, 437–470 (1996).

22. L. Gilles and B. L. Ellerbroek, "Constrained matched filtering for extended dynamic range and improved noise rejection for Shack–Hartmann wavefront sensing," Opt. Lett. 33, 1159–1161 (2008).

23. L. Gilles, L. Wang, and B. Ellerbroek, "Modeling update for the Thirty Meter Telescope laser guide star dual-conjugate adaptive optics system," Proc. SPIE 7036, 77360W-1–77360W-11 (2010).